Journal of Geodesy (2023) 97:35
https://doi.org/10.1007/s00190-023-01718-0

ORIGINAL ARTICLE

Extending the GPS IIIA antenna calibration for precise orbit determination of low Earth orbit satellites

Alex Conrad[1] · Shailen Desai[2] · Bruce Haines[2] · Penina Axelrad[1]

Received: 24 June 2022 / Accepted: 28 February 2023 / Published online: 31 March 2023

Abstract
High-precision applications of GNSS require accurate calibrations to correct for phase variations of the transmitting antennas. Calibrations distributed by the International GNSS Service (IGS), based upon observations from the global network of ground stations, are often used as the source of the transmitter calibrations as they are inherently linked to a specific definition of the International Terrestrial Reference Frame. The IGS provides antenna phase variations as a function of boresight angle for each basic block of navigation satellite. To support scientific missions operating in low Earth orbit, the antenna calibrations must be extended beyond the 14-degrees limit that can be observed by GNSS receivers on the Earth. Extended antenna calibrations to accommodate low Earth orbiting satellites have already been derived for the GPS Block II satellites. This paper derives an extension solution for the new GPS IIIA antenna calibration, based on a year of observations from the Sentinel-6 Michael Freilich altimetry mission and validated using Jason-3. These solutions are inherently consistent with the IGS-provided models of the Block II antenna calibrations. We use the new model for the GPS IIIA transmitter antenna calibration extensions to evaluate the impact on precise orbit solutions of both Sentinel-6 MF and Jason-3.

Keywords GNSS · GPS IIIA · Antenna calibration · Precise orbit determination

1 Introduction

Precise orbit determination (POD) is a fundamental component supporting the more than thirty-year long, multi-mission, sea surface height record. Because orbit radial errors map directly into the sea surface altimetry measurements, highly accurate orbit estimates are required. The first altimetry mission to apply GNSS-based precise orbit determination, TOPEX/Poseidon, was launched in 1992. Within a year, it demonstrated better than 3-cm (Bertiger et al. 1994) radial rms orbit accuracy from the Global Navigation Satellite System (GNSS) tracking data alone when processed with a reduced-dynamic technique (Wu et al. 1991; Yunck et al. 1994, 1990). The follow-on mission, Jason-1, further improved the radial rms accuracy to 1 cm by incorporating improved geopotential models and in-flight calibration of the antenna phase variations (Haines et al. 2004). Sub-centimeter accuracy for Jason-2 was achieved by also fixing phase ambiguities (Bertiger et al. 2010).

The most recent mission of the TOPEX/Poseidon and Jason series, Sentinel-6 Michael Freilich (MF), was launched on November 21, 2020, into a 66-degree inclination circular orbit with a nominal altitude of 1336 km (Donlon et al. 2021). With the goal of providing enhanced continuity of the altimetry data record (Donlon et al. 2021a), Sentinel-6 MF has been shown to achieve radial accuracies better than 1 cm (Montenbruck et al. 2021). As seen with Jason-2, this level of accuracy is highly dependent on accurate modeling of the transmitter and receiver antenna calibrations. The total antenna phase calibration is often separated into a phase center offset (PCO) and a signal line of sight phase variation (PV) with respect to the PCO, where the PCO is effectively the center of a best-fit sphere to the total phase calibration. For the remainder of this paper, we use the term antenna calibration to include the total contribution of both the PVs and the PCOs.

To achieve the most accurate POD solution, the PCO and PV modeling approach is applied to both the GNSS satellite transmitter antennas and the receiving antenna (Schmid et al. 2005, 2007). For satellite transmitters, a unique IGS PCO is

✉ Alex Conrad
alco1479@colorado.edu

[1] University of Colorado Boulder, Boulder, Colorado, USA

[2] Jet Propulsion Laboratory, California Institute of Technology, Pasadena, California, USA

provided for each satellite. The IGS PVs, however, are modeled to be identical for every satellite within a GPS sub-block and only describe variations as a function of boresight angle (Montenbruck et al. 2015). These were initially restricted to nadir angles less than 14 degrees, the limit observed for ground stations. For low Earth orbiting (LEO) satellites such as Sentinel-6 MF, however, boresight angles greater than 14 degrees are observed. Jäggi et al. (2010) proposed an extension of the IGS05 PVs beyond 14 degrees. The extension was generated from simultaneous estimation of GPS and LEO antenna calibrations using only GPS measurements collected onboard multiple LEO satellites. Later, a similar approach was also used by Schmid et al. (2016) to estimate the GPS PVs beyond 14 degrees. For several subsequent reference frame realizations, only the PCOs have been changed while the PVs have remained fixed to those provided by Jäggi et al. (2010) for IGS05. Each IGS realization of the International Terrestrial Reference Frame (ITRF) must update the transmitter PCOs due in part to the reference frame scale changes. For example, Schmid et al. (2016) estimated updated PCOs for the IGS08 definition of transmitter phase calibrations and Rebischung and Schmid (2016) updated the IGS14 values of the PCOs while continuing to adopt the PVs from IGS05.

The GPS constellation is currently in the process of incorporating new GPS IIIA transmitters, with the first satellite launched in December 2018 (Thoelert et al. 2019). As of December 2021, the GPS constellation includes 5 GPS IIIA satellites in operation with space vehicle numbers (SVN) 74 - 78. Unlike the Block II IGS14 antenna calibration that inherited the full IGS05 extension calibration values, the IGS14 GPS IIIA PVs are adopted as varying with boresight angle up to 14 degrees and then held constant for higher angles. The GPS IIIA PCO values were provided by the manufacture (Lockheed 2019) for the first GPS IIIA satellite, SVN-74. Steigenberger et al. (2020) found that these values had good agreement with on orbit estimates of the PCO. For subsequent GPS IIIA transmitters, the IGS14 adopted the SVN-74 PCO values. The Block II IGS antenna calibrations are separated into six sub-block groups: II, IIA, IIR-A, IIR-B, IIR-M, and IIF. For the remainder of this paper, we collectively refer to all these sub-blocks as Block II while applying the specific IGS14 sub-block PVs and individual PCOs. Additionally, for the purposes of comparison the sub-block types IIR-B and IIR-M are combined due to having identical IGS14 PVs.

In this study, we aim to generate an extension of the IGS14 GPS IIIA PVs for boresight angles higher than 14 degrees that is consistent with the Block II antenna calibrations. This approach facilitates the continuity of POD solutions based on IGS standards during and after the transition of the GPS constellation from Block II to GPS IIIA transmitters. To extend the GPS IIIA antenna calibrations above 14 degrees, we use the Sentinel-6 MF GPS L1/L2 carrier and pseudorange observations from the TriG receiver (Donlon et al. 2021). At the nominal altitude of 1336 km, Sentinel-6 MF routinely observes GPS measurements with boresight angles greater than 14 degrees. Sentinel-6 MF is an ideal platform for extending the GPS IIIA antenna calibration because of its altitude, geodetic quality receivers and antennas with favorable multipath and demonstrated radial orbit accuracy better than 1 cm rms. Additionally, during the majority of 2021, Sentinel-6 MF was flying in tandem with Jason-3 where it is following the same ground track, but approximately 30 s behind (Donlon et al. 2021a). Thus, we can use Jason-3 to validate the Sentinel-6 MF derived GPS IIIA antenna calibration extension.

To produce a GPS IIIA antenna calibration extension consistent with the IGS14 Block IIs, we implement the following approach. We first generate a Sentinel-6 MF receiving antenna calibration based only on GPS Block II tracking data and using the IGS14 definition of the transmitter antenna calibrations. With this receiver antenna calibration, Block II based dynamic orbit and clock solutions for Sentinel-6 MF are estimated. We then use residuals from the withheld GPS IIIA tracking data and predicted observables based on the dynamic orbit and clock solutions to determine the GPS IIIA dependency on boresight angle, namely the PV. The IGS14 definition of the PCO is held fixed. Finally, to test the fidelity of the proposed extension, we compare orbit solutions with and without GPS IIIA satellites for Jason-3 - a LEO satellite not used in the calibration procedure.

In this paper, Sect. 2 describes the POD models and solution strategy, the Sentinel-6 MF receiver antenna calibration method, and the GPS IIIA antenna calibration extension process. In Sect. 3 we assess the validity of the calibration by comparing orbit metrics for three different scenarios. The first POD solution uses only Block II measurements; the second includes Block II and IIIA measurements with the original IGS14 antenna calibrations; and finally the third includes Block II and IIIA measurements with the newly generated antenna calibration extension. Section 4 describes validation of the GPS IIIA calibration extension using Jason-3 as an independent platform. In Sect. 5 we provide the overall conclusions and recommendations.

2 Methods

2.1 Sentinel-6 MF instrumentation

Sentinel-6 MF is equipped with four independent tracking systems for POD, a Doppler Orbitography and Radiopositioning Integrated by Satellite (DORIS) receiver (Auriol and Tourain 2010), retro-reflectors for ground-based satellite laser ranging (SLR), a redundant multi-GNSS PODRIX receiver from RUAG that is the primary GNSS POD instrument for this satellite, and a TriG POD receiver from

NASA/JPL that also supports radio occultation measurements. POD based on data from GPS/Galileo with the primary multi-GNSS PODRIX receiver from RUAG has already been presented by Montenbruck et al. (2021). The TriG draws its heritage from the NASA/JPL BlackJack receiver line, which has set accuracy standards for the Jason-series of reference altimeter missions preceding Sentinel-6 MF (Haines et al. 2004; Bertiger et al. 2010; Young 2017). On Sentinel-6 MF, the TriG is providing multi-GNSS tracking data from forward- and aft-facing radio-occultation antennas and GPS tracking data from an upward facing POD antenna (Tien et al. 2010; Tien et al. 2012). Our Sentinel-6 MF POD exclusively uses the undifferenced GPS L1/L2 pseudorange and carrier measurements received by TriG POD antenna. For this analysis, the TriG measurements are preferable for a few reasons. First, observations are tracked down to 0-degrees elevation whereas the PODRIX enforces a cut off at 10 degrees. These low elevation measurements in the receiver frame result in more observations in transmitter boresight angles above 14 degrees. Second, because the Trig only tracks GPS signals (PODRIX tracks both GPS and Galileo), this allows for a more robust Block II only solution due to significantly more GPS measurements. In a manner similar to Bertiger et al. (2010), the raw 1Hz measurements are decimated to a 5-minute dual-frequency (ionosphere-free) combination for the GPS carrier and pseudorange (LC and PC) observations.

2.2 Orbit models/solution strategy

We used JPL's GipsyX/RTGx software (Bertiger et al. 2020) for all of our precise orbit determination solutions. Table 1 provides an overview of the models applied for each POD solution. The only exception to this is for the antenna calibration estimation strategy which uses 24-hour arcs and 30-second observations.

We use a custom 12-panel macromodel (Conrad et al. 2022), described in Table 2, along with measured spacecraft attitude to compute the drag and solar radiation forces. The drag incorporates the DTM2000 model to estimate the atmospheric density from the F10.7 cm solar flux and the Kp geomagnetic indices (Bruinsma et al. 2003). Radiation pressure forces for both Earth albedo (Knocke et al. 1988) and visible solar (Milani et al. 1987) are applied. The geopotential is computed using the GRACE time-variable CNES/GRGS RL04 Earth gravity models up to degree and order 200 (Lemoine et al. 2019). Additional gravitational effects such as solid Earth tides and pole tides conform to the version 1.3.0 IERS conventions (Petit and Luzum 2010). Ocean tides use a GOT4.8a model (Ray 2013) modified to account for geocenter motion (Desai and Ray 2014), and implemented using the convolution formalism of (Desai and Yuan 2006). Third-body gravitational effects are included using the JPL DE421 planetary and lunar ephemeris (Folkner et al. 2009).

GPS satellite ephemerides, clock solutions, widelane phase bias information, as well Earth orientation parameters come from the JPL IGS analysis center final products (Dietrich et al. 2018). Based on the IGS standards (Johnston et al. 2017), the GPS clock solutions are referenced to the L1/L2 P(Y)-code dual-frequency ionosphere-free combination. Orbit solutions and background models applied the IGS14 reference frame which is the IGS realization of the ITRF14 (Altamimi et al. 2016). We used the IGS14 GPS antenna calibrations, including both PCOs and PVs, except for where we specifically note that we have applied our new estimates of the GPS IIIA extensions for boresight angles larger than 14 degrees.

Different orbit determination strategies are used for each stage of the solution. When deriving the antenna calibration, we adopt a dynamic POD approach estimating once per revolution empirical parameters fixed over a daily solution. Our most rigorous solutions adopt a reduced dynamic POD approach, where we follow the dynamic solutions with reduced dynamic solutions that estimate stochastically varying empirical accelerations with phase ambiguity resolution (Bertiger et al. 2010). These are summarized in Table 3. These reduced dynamic and ambiguity resolved solutions are the basis for evaluation of the GPS IIIA antenna calibration extension.

2.3 Sentinel-6 MF antenna calibration

The Sentinel-6 MF TriG receiver antenna calibration is generated using only the GPS Block II measurements. Without some judicious constraint, it is not possible to fully decouple the receiver antenna calibration from transmitter antenna calibration. This approach effectively ties the Sentinel-6 MF antenna calibration to the established IGS14 transmitter calibrations. The receiver antenna calibration is estimated from daily solutions generated from 24-hour dynamic orbit estimates (including daily estimates of drag coefficient and once per revolution accelerations in cross-track and in-track). We first perform a daily orbit solution using the pre-launch measurements of the receiver calibration and with all Block II tracking data. From this solution, we identify outliers which are then excluded from a subsequent dynamic orbit solution that also simultaneously estimates a two-dimensional receiver antenna calibration correction to the pre-launch receiver calibration. The estimated antenna calibration correction is defined as discrete bins of 3 degrees in elevation and 4 degrees in azimuth for elevations below 51 degrees. Above this, the azimuth bin spacing is variable to account for lower measurement density at higher elevations. Outliers are removed as they can significantly influence the receiver calibration, especially for bins with low measurement den-

Table 1 Measurement and POD models applied in GipsyX/RTGx

Model/parameter	Sentinel-6 MF selection
GNSS observations	Undifferenced GPS L1/L2 phase and pseudorange 5-min observations, 30-hour daily arcs
Surface forces	Custom macromodel (Table 2)
Sentinel-6 mass	1180.633 kg (Jan 1, 2021)
Sentinel-6 attitude	Measurement quaternions
Sentinel-6 TriG antenna Reference point	[−0.933048, 0.006592, −1.13205] m, (Jan 1, 2021)
Atmospheric density	DTM2000 (Bruinsma et al. 2003)
GPS satellite antenna calibrations	IGS14 Values (igs14_2194.atx) (Rebischung and Schmid 2016)
Earth orientation/rotation	JPL IGS Analysis center IGS14 final solutions
GPS spacecraft ephemerides	JPL IGS Analysis center IGS14 final solutions
GPS spacecraft clocks and widelane Phase bias information	JPL IGS analysis center IGS14 final solutions
Planetary and lunar ephemerides	JPL DE421 ephemerides (Folkner et al. 2009)
Earth gravity field	EIGEN-GRGS.RL04.MEAN-FIELD (Lemoine et al. 2019)
Ocean tides	GOT4.8 tide model (Ray 2013)
Reference frame	IGS14

Table 2 Custom 12-surface macromodel

Surface	Surface normal [x,y,z]	Area (m^2)	Diffusivity	Specularity
Body +X	[1.000, 0.000, 0.000]	4.149	0.041	0.349
Body -X	[−1.000, 0.000, 0.000]	3.941	0.042	0.546
Body +Y	[0.000, 1.000, 0.000]	1.329	0.040	0.506
Body -Y	[0.000, −1.000, 0.000]	1.329	0.040	0.506
Body +Z	[0.000, 0.000, 1.000]	11.830	0.016	0.571
Body -Z	[0.000, 0.000, −1.000]	2.072	0.030	0.660
Left SP	[0.000, −0.616, −0.788]	8.65	0.316	0.139
Right SP	[0.000, 0.616, −0.788]	8.65	0.316	0.139
AMR-C (top)	[0.469, 0.000, −0.883]	0.92	0.080	0.000
AMR-C (bottom)	[0.000, 0.000, 1.000]	0.8123	0.563	0.188
Left SP (bottom)	[0.000, −0.616, 0.788]	3.760	0.164	0.013
Right SP (bottom)	[0.000, 0.616, 0.788]	3.760	0.164	0.013

sity. The sum of the pre-launch calibration and the estimated correction then forms the total receiver antenna calibration which corrects for line-of-sight variations due to antenna gain patterns and spacecraft multipath.

The antenna calibration can be formulated in terms of the mean PCO and a set of line-of-sight azimuth and elevation dependent antenna calibrations. Rothacher et al. (1995) showed that there are inherent degrees of freedom for a phase center offset vector $\mathbf{r}_0$ and antenna calibration function $\phi(\alpha, z)$ and can be transformed into a new PCO and antenna calibration function using the following:

$$\mathbf{r}_0' = \mathbf{r}_0 + \Delta\mathbf{r} \tag{1}$$

$$\phi'(\alpha, z) = \phi(\alpha, z) - \Delta\mathbf{r} \cdot \mathbf{e} + \Delta\phi \tag{2}$$

where Δr and $\Delta\phi$ can be chosen arbitrarily and $\mathbf{e}$ is a unit vector in the line of sight direction from the receiver to the transmitter. Because $\Delta\phi$ cannot be separated from the receiver clock, it must be constrained. This is often done by constraining the boresight direction to zero, but due to the low density of observations for LEO spacecraft in the boresight direction, we instead choose to level the entire antenna calibration correction by constraining the average of all bins above 30-degrees elevation to zero. Given that Sentinel-6 MF is roughly yaw-fixed relative to the flight direction, it is difficult to resolve a mean PCO due to the phase variations

Table 3 POD estimation strategy within GipsyX/RTGx

Estimated parameters	Parameterization	*a priori* σ
Epoch state		
3-D epoch position (X,Y,Z)	Bias per arc	10 km
3-D epoch velocity (X,Y,Z)	Bias per arc	1 km/s
Empirical Acceleration (3 dynamic passes)		
Drag Coefficient	Bias per arc	1000
Once-per-rev cross-track (cos, sin)	Bias per arc	1 mm/s^2
Once-per-rev in-track (cos, sin)	Bias per arc	1 mm/s
Empirical Acceleration (reduced-dynamic)		
Radial	Stochastic with τ = 6 hrs Δt = 30 min	1 nm/s^2
In-track	Stochastic with τ = 6 hrs Δt = 30 min	1 nm/s^2
Once-per-rev cross-track (cos, sin)	Stochastic with τ = 6 hrs Δt = orbit	2 nm/s^2
Once-per-rev in-track (cos, sin)	Stochastic with τ = 6 hrs Δt = orbit	2 nm/s^2
Carrier Phase Bias	Constant bias per continuous carrier track	1e6 km
TriG Clock Offset	White-noise Process	3e5 km

Δt is the update interval and τ is the correlation time

relative to the antenna reference point for the in-track (body-x direction) direction. This issue has previously been observed in estimation of the horizontal PCOs for GNSS satellites during periods when the spacecraft attitude aligns the body x- or y-axis with the in-track direction (Schmid et al. 2007; Huang et al. 2022). For this reason, we also choose to constrain the PCO of the antenna calibration correction in the body-x direction to zero. This is equivalent to $\Delta\mathbf{r} = [\Delta x = 0, \Delta y, \Delta z]$. Here we allow the receiver antenna calibration to absorb offsets in the body-y and z components relative to the *a priori* values, but not for the body-x offset.

Because the Sentinel-6 MF attitude is roughly yaw-fixed, non-gravitational modeling errors in the cross-track direction can influence the antenna y-offset estimates. Specifically, solar radiation pressure modeling errors are expected to produce y-offset estimates that correlate with seasonal changes in the beta angle (sun elevation relative to orbit plane). To mitigate errors in the y-offset, we use a tuned custom macro-model. We also examine a sampling period that is long enough to reduce the beta angle dependent errors in the final solution. We then combine the daily normal equations from 388 (after outlier removal) days (2021-01-01 to 2022-02-13) to determine the antenna calibration correction. Given that the beta angle cycle is roughly 120 days for Sentinel-6 MF, this results in just over three full cycles. The final Sentinel-6 MF antenna calibration is generated by accumulating the final square root information filter (SRIF) state output from each Block II only daily solution into a single estimate from the accumulated time frame. It is during this process that the average of all bins above 30-degrees elevation and body-x offset are constrained to zero.

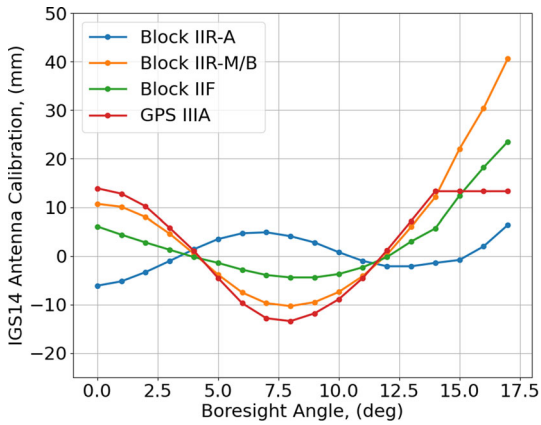

Fig. 1 IGS14 PVs as a function of boresight angle separated by block type from igs14_2194.atx. Note: Block IIR-B antenna PVs are the same as IIR-M

2.4 GPS IIIA antenna calibration extension

Unlike the Block II variants, the current IGS14 GPS IIIA antenna calibrations above 14 degrees, as seen in Fig. 1, are fixed to the value from the 14-degree boresight angle. Here we describe the approach taken to extend them to 17 degrees.

We note that JPL's Final orbit and clock solutions for the GPS constellation are determined from a global ground network. Because of this, the GPS orbit and clock products only depend on the IGS14 calibration values for boresight angles less than 14 degrees. For this reason, we choose to limit our modification of the IGS14 GPS IIIA calibration values to boresight angles greater than 14 degrees to improve the LEO POD without affecting terrestrial GNSS processing with IGS14 values.

To ensure the GPS IIIA antenna calibration extension is derived relative to the Block II, a two-iteration process is implemented. First, Sentinel-6 MF dynamic orbits are computed using only Block II measurements and our computed receiver antenna calibration. The orbit and receiver clock solutions are then fixed, and the GPS IIIA dual-frequency phase measurements are fit to those Block II-based dynamic orbit solutions estimating only a phase arc bias. The resulting GPS IIIA residuals are zero mean across all boresight angles. This results in an undesired mean residual offset below 14 degrees that is due primarily to poorly modeled calibration values above 14 degrees. To facilitate a consistent calibration for the higher boresight angles, the stacked GPS IIIA residuals are offset such that their mean value below 14 degrees over the entire dataset is zero. From this starting point, we iterate a solution based on the fixed Block II orbits and clock solution with updates to the GPS IIIA antenna calibration above 14 degrees based on stacked post-fit residuals. Our approach ensures that the new GPS IIIA antenna calibration extensions are consistent with the IGS14 Block II antenna calibrations.

3 Results

We use the TriG receiver GPS L1/L2 5-minute decimated phase and pseudorange measurements from the entirety of 2021 for all subsequent results, the exception being the estimation of the antenna calibration which uses 30-second data over a slightly longer time span. The following sections first describe the resulting receiver antenna calibration and GPS IIIA satellite antenna calibration extension estimated from 24-hour solutions. We evaluate the consistency of the GPS IIIA antenna calibration extension by comparing reduced-dynamic ambiguity resolved 30-hour precise orbit solutions from three cases: using only Block II tracking data with IGS14 antenna calibration, using Block II and IIIA tracking data with default IGS14 antenna calibration, and using Block II and IIIA tracking data with IGS14 calibration modified to include our extensions above 14-degree boresight angles. Orbit quality is evaluated using comparisons of internal metrics. The statistics for the daily solutions are reported in terms of the mean value $\pm$ the standard deviation of the full year of daily solutions. Finally, withheld SLR measurements are independently applied to evaluate the orbit solution accuracy for all three scenarios.

3.1 Antenna calibrations

3.1.1 Sentinel-6 MF antenna calibration

The Sentinel-6 MF antenna calibration is generated from more than one year of data spanning from 2021-01-01 to 2022-02-13. High-rate 30-second L1/L2 ionosphere-free dual-frequency combination observations from Block II only measurements for the phase and P(Y)-code measurements are applied. Daily solutions with fewer than 18,000 phase measurements and daily rms of post-fit phase residuals above 5.5 mm, along with days that have orbit maintenance maneuvers, are excluded from the final estimate of the receiver calibration resulting in a total of 388 daily solutions. The final estimated antenna calibrations are generated for both phase and code solutions. Figure 2 shows a comparison of the L1/L2 dual-frequency phase pre-launch anechoic chamber antenna calibration, the estimated correction, and the resulting in-flight Block II derived antenna calibration. The antenna calibration values are described using azimuth measured clockwise from 0 to 360-deg and elevation from 0 to 90-deg in the antenna frame which is closely aligned with the spacecraft body x/y/z frame. The 0-deg azimuth direction corresponds to the positive antenna-x direction (body +x), 90-deg azimuth to the negative antenna-y direction (body +y), and 90-deg elevation to the positive antenna-z direction (body -z). As expected, the overall structure is similar between the original and the final, but there is significant irregular structure with variations on the order of -20 to 10 mm in portions of the antenna calibration captured in the in-flight environment, presumable due to multipath and a significant z-PCO contribution. When compared to the pre-launch antenna calibration, the resulting PCO offsets in the antenna y and z directions are -3.8 mm and -20.0 mm, respectively. For our implementation, we do not separate out the PCO from the estimated calibration, but rather retain the antenna reference point in Table 1 and allow the antenna calibration to absorb the estimated offsets.

A consideration for the use of high-rate data is due to the yaw-fixed attitude of Sentinel-6 MF. This results in relatively few measurements for elevations below 6 degrees in the in-flight direction, making this portion of the antenna calibration much more difficult to resolve. For the time-span contributing to the antenna calibration, there are three instances where the nominal yaw attitude is flipped 180 degrees for a few days. The high-rate data combined with the yaw-flip maneuvers allow for much better resolution of the low elevation portion of the antenna calibration in the nominal flight direction (azimuth = 0°).

3.1.2 GPS IIIA antenna calibration extension

With the Sentinel-6 MF receiver antenna calibration established based on the Block II calibrations, we are able to compute a GPS IIIA transmitter extension consistent with the Block II IGS14 antenna calibrations. From each daily Block II derived dynamic orbits solutions during 2021, GPS IIIA residuals from five transmitters (SVNs 74-78) are fit and then stacked by boresight angle. Days with orbit maintenance maneuvers are excluded. Figure 3 shows the stacked residuals with a bin size of 0.25 degrees from post-fit measurement residuals and the right panel shows the number of residuals in each bin. The GPS IIIA observations contribute 13.2% of the total number of observations over all boresight angles. However, more than half of the GPS IIIA observations occur above 14 degrees boresight angles. An improved antenna calibration above 14 degrees, instead of the simple approach of using the value from 14 degrees, is therefore an important improvement to the Block IIIA measurement model. In contrast, the Block II stacked residuals do not indicate significant deficiencies. We use the mean stacked residuals from the 0.25 degree bins to derive GPS IIIA extension at boresight angles of 15, 16, and 17 degrees as shown in Table 4. The resulting GPS IIIA extension after convergence is shown in Fig. 4.

We note also that our estimated extension of the GPS IIIA PVs is very similar to that of the Block IIR-M constellation from IGS14. Using that extension is a potential alternative to the values we proposed in Table 4. The two platforms are both manufactured by Lockheed Martin which may explain some of the similarity. Additionally, Steigenberger et al. (2020) found agreement in other aspects such as the attitude profile and dimensions.

3.2 Orbit quality comparison

3.2.1 Sentinel-6 MF internal metrics

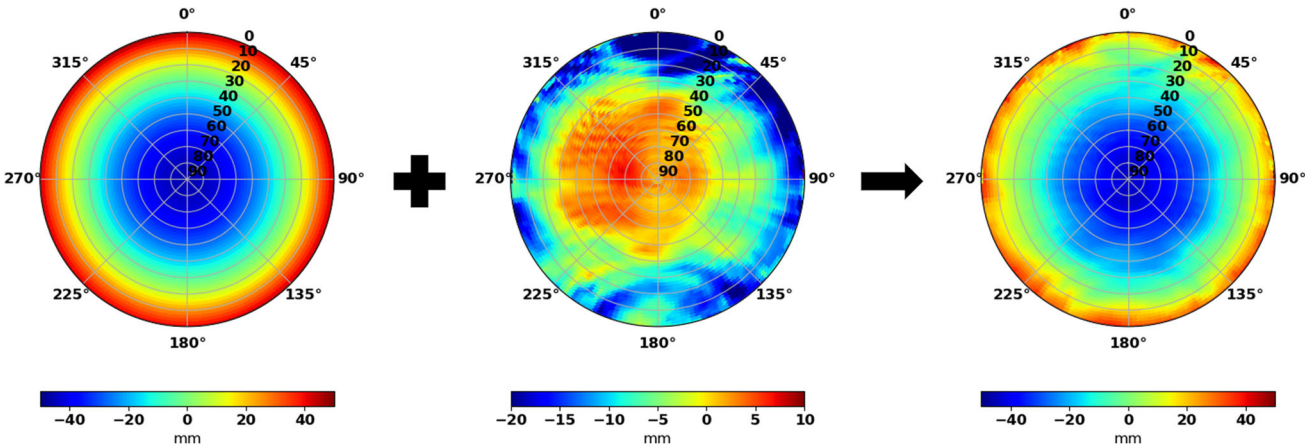

Fig. 2 Pre-launch phase antenna calibration (left) combined with the estimated antenna calibration correction (middle) and resulting in-flight Block II derived phase antenna calibration (right)

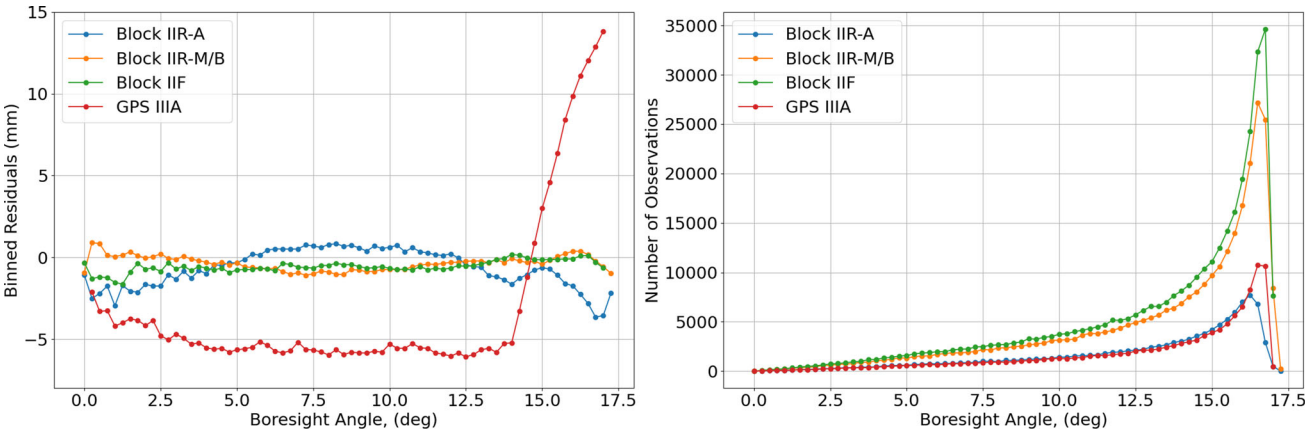

Fig. 3 Stacked residuals relative to Block II-only orbit solutions (left) and the total number of observations in each bin (right) for Block IIR-A (blue), IIR-M/B (orange), IIF (green), and IIIA (red)

Table 4 Estimated GPS IIIA antenna calibration extension values

Boresight angle	14 degrees	15 degrees	16 degrees	17 degrees
Calibration value	13.3 mm	23.9 mm	33.9 mm	42.4 mm

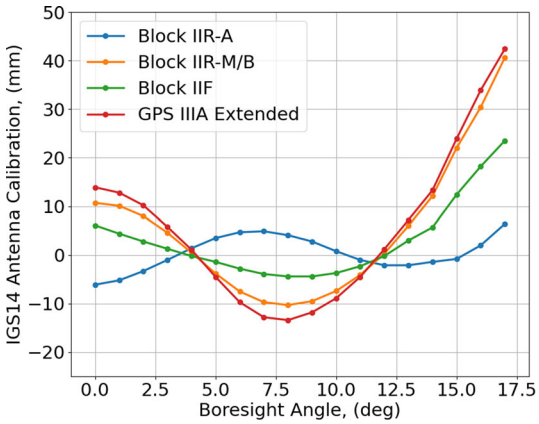

Fig. 4 GPS IIIA extended PV (red) as a function of boresight angle compared to existing IGS14 Block IIR-A (blue), IIR-M/B (orange), and IIF (green) PVs

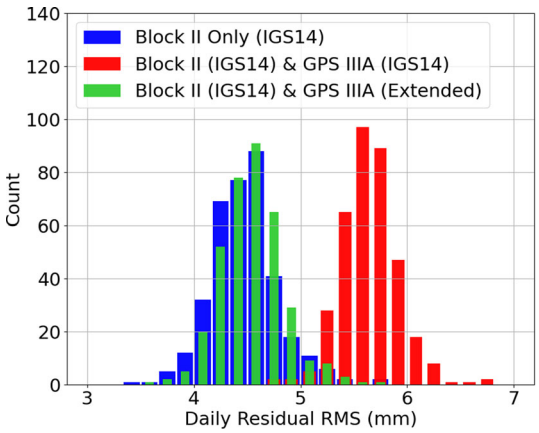

Fig. 5 RMS of Postift LC residuals from Sentinel-6 MF ambiguity-resolved reduced dynamic orbit solutions for three cases: 1) Block II tracking data alone (blue), 2) Block II and IIIA tracking data with IGS14 antenna calibrations (red), 3) same as case (2) but using GPS IIIA PV extension (green)

The daily ionosphere-free dual-frequency phase post-fit residual rms is an indicator of the goodness-of-fit of the orbit solution and will be impacted by how well the receiving and transmitting antennas are modeled. Figure 5 shows the histogram of daily rms of postfit phase residuals from daily 30-hour reduced dynamic POD solutions from the entirety of 2021. As expected, our GPS IIIA antenna calibration extensions clearly provide a better fit to the data. Most notably, the postfit rms of residuals from POD solutions using both Block II and IIIA tracking data fall in-line with solutions using only Block II tracking data. Meanwhile, and as also shown in Table 5, POD solutions using Block II and IIIA tracking data with the IGS14 antenna calibrations as provided are higher by 20%. Looking only at the GPS IIIA data shows a more than 50% reduction in the postfit residual rms when using our GPS IIIA extension.

From daily 30-hour ambiguity resolved orbit solutions, there are six hours of overlap. Here we difference the central four hours to compute a single daily radial, cross-track, and in-track component rms statistic. The resulting rms values are a measure of the orbit solution precision and consistency. Daily rms values that are more than 5 standard deviations away from the overall mean value are removed. Figure 6 shows the daily overlap statistics histogram for each component. Computing the mean and standard deviation of all daily overlap difference rms statistics produces a way to evaluate the overall precision and consistency of the solutions. Table 6 lists the mean values and standard deviation for all three components. Overall, the orbit solutions that incorporate the GPS IIIA measurements with the extrapolated antenna calibration show an improved orbit solution precision with slightly lower overlap statistics for all three components, in both the mean and standard deviation of daily values. Of course, the GPS constellation currently only includes 5 GPS IIIA satellites, and we would expect higher impact as that number continues to increase. Given that the orbit overlaps are a measure on solution precision, we would expect the reduced dynamic approach to result in similar results. The improvement when including GPS IIIA measurements is due in part to the increased number of measurements, as compared to when they are excluded

3.2.2 Ambiguity resolution

Each of the daily reduced dynamic POD solutions includes an ambiguity resolution summary. Fixed phase ambiguity biases are applied within the filter smoother using a constraint with a confidence level of 10 cm. Figure 7 shows the distribution of passes with narrow-lanes (NL) constrained to less than 10 centicycles of the fixed ambiguity. The Block II only orbit solutions have a median of 84.5 percent of NL passes constrained to less than 10 centicycles while the inclusion of the GPS IIIA with the IGS14 antenna calibrations reduces the median to 82.7 percent. Using the extended GPS IIIA antenna calibration brings the median back to 84.5 percent of passes constrained to less than 10 centicycles. Here we see that by extending the GPS IIIA IGS14 antenna calibra-

Table 5 Sentinel-6 MF mean values ± the standard deviation of all daily residual rms

	LC (mm)	LC GPS IIIA Only (mm)	PC (mm)
Block II Only	4.5 ± 0.32	–	622 ± 61
Block II and IIIA IGS14	5.6 ± 0.27	9.7 ± 0.45	609 ± 110
Block II and IIIA Extended	4.5 ± 0.30	4.5 ± 0.52	609 ± 100

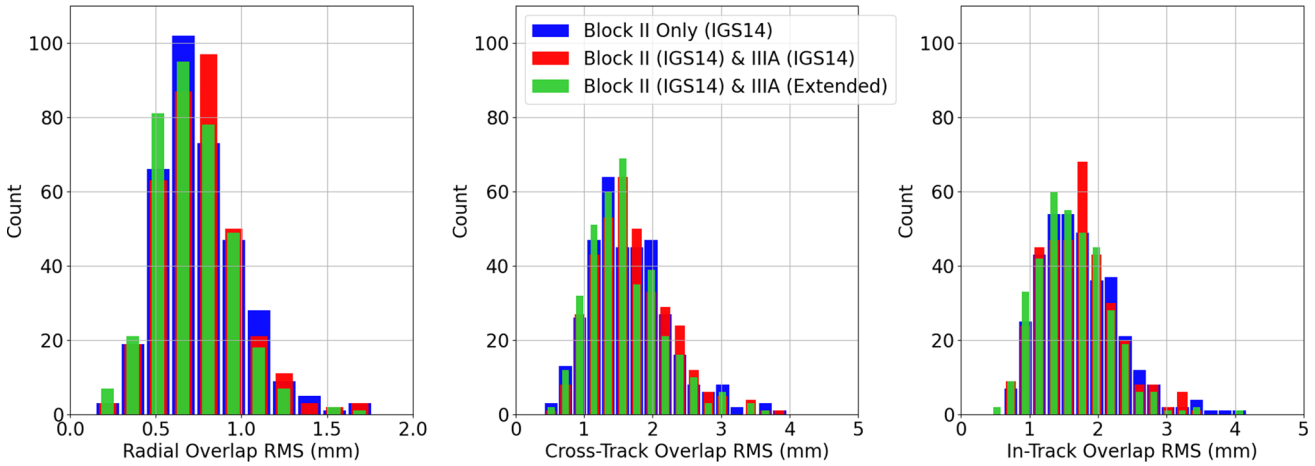

Fig. 6 Daily overlap difference RMS for radial (left), cross-track (middle), and in-track (right) from Sentinel-6 MF ambiguity-resolved reduced dynamic orbit solutions for three cases: 1) Block II tracking data alone (blue), 2) Block II and IIIA tracking data with IGS14 antenna calibrations (red), 3) same as case (2) but using GPS IIIA PV extension (green)

Table 6 Mean values ± the standard deviation of the daily component overlap difference rms

	Radial (mm)	Cross-track (mm)	In-track (mm)
Block II Only	0.78 ± 0.33	1.7 ± 0.57	1.8 ± 1.0
Block II and IIIA IGS14	0.77 ± 0.31	1.7 ± 0.56	1.8 ± 0.90
Block II and IIIA Extended	0.73 ± 0.28	1.6 ± 0.54	1.7 ± 0.83

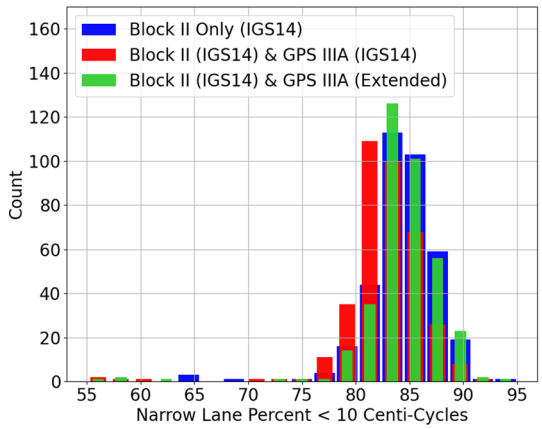

Fig. 7 Daily narrow lane ambiguity resolution histogram of percent constrained to less than 10 centi-cycles from Sentinel-6 MF ambiguity-resolved reduced dynamic orbit solutions for three cases: 1) Block II tracking data alone (blue), 2) Block II and IIIA tracking data with IGS14 antenna calibrations (red), 3) same as case (2) but using GPS IIIA PV extension (green)

tion the ambiguity resolution improves and is consistent with the Block II only results.

3.2.3 External metrics

To evaluate the orbit accuracy, we consider independent SLR measurements (Pearlman et al. 2019). Only SLR stations with biases below 5 mm for the entire dataset are analyzed. These include a total of eight stations: Greenbelt, Maryland; Graz, Austria; Herstmonceux, UK; Hartebeesthoek, South Africa; Mt Stromlo, Australia; Yarragadee, Australia; Wettzell, Germany; and Zimmerwald, Switzerland. Figure 8 shows the SLR residual rms, left panel, and overall bias, right panel, from all SLR measurements across 2021 as a function of boresight angle relative to the SLR frame. Here we can see that all three orbit solutions are relatively similar. Overall rms values are 8.9 mm for Block II only, 8.9 mm including GPS IIIA with IGS14 antenna calibrations, and 8.8 mm including GPS IIIA with extended antenna calibration. The consistency in the SLR residuals

Table 7 Comparison of the overall rms, bias, and standard deviation of the SLR residuals

	RMS (mm)	Bias (mm)	Std (mm)
Block II only	8.9	1.26	8.8
Block II and IIIA IGS14	8.9	0.99	8.8
Block II and IIIA extended	8.8	1.28	8.7

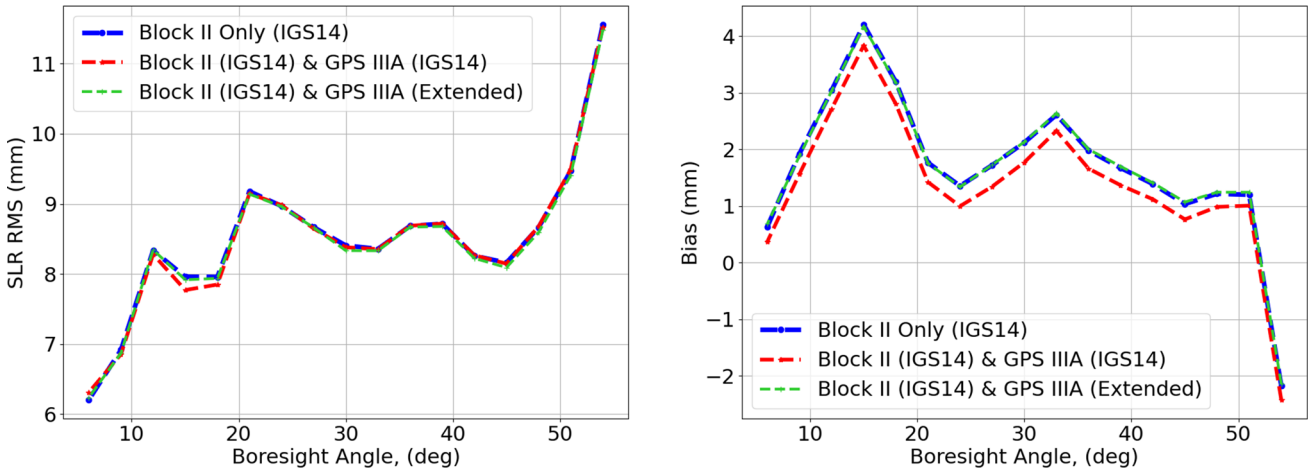

Fig. 8 SLR residual RMS (left) and bias (right) as a function of boresight angle

rms values between all three solutions is likely due to the strength of the ambiguity resolution of the Block II measurements which contribute more than 85 percent of the total measurements. It is reasonable to conclude, that as the number of GPS IIIA satellites increase, the orbit accuracy will be degraded without extension of the GPS IIIA calibration.

Looking at the SLR residual bias as a function of boresight angle shows a shift of about 0.3 mm when using the GPS IIIA measurements with IGS14 antenna calibrations. Incorporating the GPS IIIA measurements with the extended antenna calibration produces SLR biases that are essentially consistent with the Block II only solutions. Table 7 shows a comparison of the overall statistics from each set of orbit solutions.

4 Independent validation with Jason-3

The GPS IIIA extensions are validated using Jason-3 by applying the same three scenarios as those above with Sentinel-6: a Block II only solution, a Block II and IIIA solution using IGS14 antenna calibrations for both, and finally, a Block II and IIIA solution with extended GPS IIIA calibration. Worth noting is that the Jason-3 GPS antenna is tilted 15 degrees away from zenith while the Sentinel-6 GPS antenna points towards zenith. This combined with a yaw-steering attitude profile changes the correlation between the receiver and transmitters, particularly the z-PCOs. As such, Jason-3 provides a useful validation of the consistency of the GPS IIIA PV extension given that is has different lines of sight to the GPS constellation. These solutions are processed over the same time frame as the previous Sentinel-6 MF results, 2021-01-01 to 2021-12-31. Like Sentinel-6 MF, the Jason-3 receiver calibration is generated from Block II only measurements although from a longer time frame covering from 2016-02-13 to 2020-09-12.

4.1 Jason-3 internal metrics

The Jason-3 daily L1/L2 dual-frequency phase post-fit residual rms is shown in Fig. 9. Here the results show a pattern that matches what was observed in Sentinel-6 MF, where the POD solutions using both Block II and IIIA tracking data are more inline with Block II-only solutions when the extended calibrations for the GPS IIIA transmitters are applied.

Comparing the daily central four hours of overlap differences for radial, cross-track, and in-track components, we observe a similar pattern to the Sentinel-6 MF overlap statistics. As with Sentinel-6 MF, outliers 5 standard deviations from the mean are removed. Figure 10 shows the daily overlap statistics for all three solutions. Table 9 lists the mean values $\pm$ the standard deviation for all daily overlap values. While the overall improvements to the mean values are relatively small when using the extended GPS IIIA calibration, it does represent an improvement to the POD solution. The improvement to the standard deviations suggests a better day-to-day consistency, particularly for the in-track component.

Table 8 Jason-3 mean values ± the standard deviation of the daily residual rms fit

	LC (mm)	LC GPS IIIA Only (mm)	PC (mm)
Block II only	4.4 ± 0.25	–	378 ± 27
Block II and IIIA IGS14	5.6 ± 0.38	9.3 ± 1.0	391 ± 26
Block II and IIIA extended	4.5 ± 0.24	4.6 ± 0.40	390 ± 26

Table 9 Jason-3 mean values ± the standard deviation of the daily component overlap difference rms

	Radial overlap (mm)	Cross-track (mm)	In-track (mm)
Block II only	0.80 ± 0.29	1.7 ± 0.61	1.8 ± 0.72
Block II and IIIA IGS14	0.79 ± 0.26	1.7 ± 0.58	1.8 ± 0.62
Block II and IIIA extended	0.76 ± 0.26	1.7 ± 0.55	1.7 ± 0.62

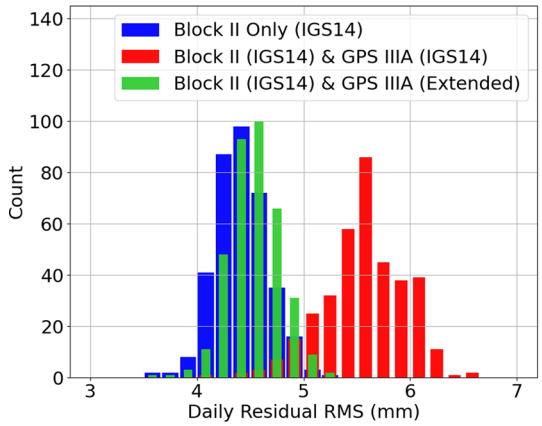

Fig. 9 RMS of Postfit LC residuals from Jason-3 ambiguity-resolved reduced dynamic orbit solutions for three cases: (1) Block II tracking data alone (blue), (2) Block II and IIIA tracking data with IGS14 antenna calibrations (red), (3) same as case (2) but using GPS IIIA PV extension (green)

4.2 Jason-3 ambiguity resolution

Once again, the daily NL ambiguity resolution statistics for Jason-3 show a similar pattern when compared to the Sentinel-6 MF ambiguity resolution. Figure 11 shows the statistics of the daily ambiguity resolution across all of 2021. The median value of NL passes that are fixed to less than 10 centi-cycles is 90.3 percent for the Block II only orbit solutions, 89.0 when including GPS IIIA with IGS14 calibration, and 90.4 percent including GPS IIIA with extended calibration. Here the ambiguity resolution with the extended GPS IIIA antenna calibrations is consistent with the Block II only results.

4.3 GPS transmitter calibrations

To evaluate the overall consistency of the transmitter antenna calibrations, residuals are stacked by boresight angle and separated into sub-block types for all of 2021. Figure 12 shows

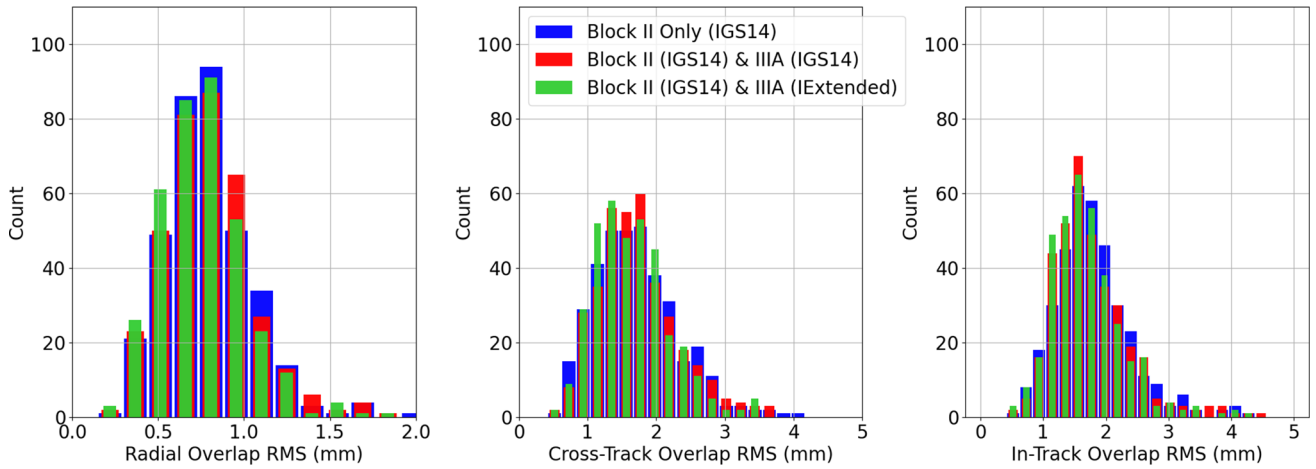

Fig. 10 Jason-3 Daily overlap RMS for radial (left), cross-track (middle), and in-track (right) from Jason-3 ambiguity-resolved reduced dynamic orbit solutions for three cases: (1) Block II tracking data alone (blue), (2) Block II and IIIA tracking data with IGS14 antenna calibrations (red), (3) same as case (2) but using GPS IIIA PV extension (green)

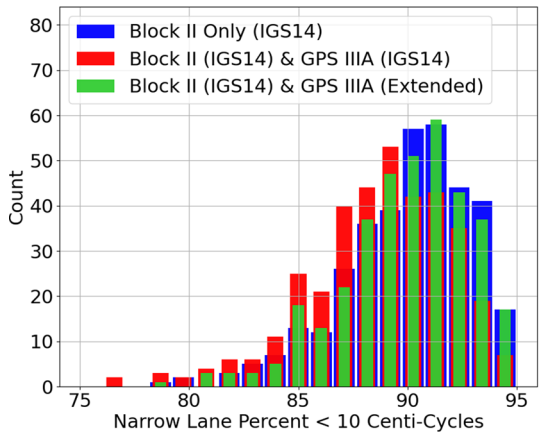

Fig. 11 Daily narrow lane ambiguity resolution histogram of percent constrained to less than 10 centi-cycles from Jason-3 ambiguity-resolved reduced dynamic orbit solutions for three cases: (1) Block II tracking data alone (blue), (2) Block II and IIIA tracking data with IGS14 antenna calibrations (red), (3) same as case (2) but using GPS IIIA PV extension (green)

the mean residual value for both Sentinel-6 MF (left) and Jason-3 (right) as a function of transmitter boresight angle from the reduced dynamic and ambiguity resolved solutions with the GPS IIIA antenna calibration extension. The GPS IIIA satellite stacked residuals are generally quite consistent between the Jason-3 and Sentinel-6 MF solutions across all boresight angles less than 17 degrees, despite them being processed completely independently of each other, and each with their own receiver antenna calibrations. There are differences on the order of 1-2 mm at boresight angles higher than 17 degrees. These results suggest that improvements on the order of 1-2 mm to the IGS14 PVs at all boresight angles for all blocks could be possible. The poorer performance of the IIR-A residuals may be due to the IGS14 antenna calibration estimate being relative to a group of satellites that have now been partially phased out of operation, showing potential a weakness in applying combined PVs to an entire transmitter sub-block.

4.4 Manufacture published PVs for GPS IIIA

A recent public release of measured antenna patterns for the first five GPS IIIA satellites (Fischer 2022) provides an opportunity for comparison with the extended GPS IIIA IGS14 PVs derived in this work. The dataset, which includes phase measurements across azimuth and boresight angles for each operational frequency (L1, L2, and L5), was collected prior to antenna installation on the spacecraft. To compare against the GPS IIIA IGS14 PVs, phase values are converted to length and averaged across azimuth. The individual L1 and L2 patterns are then combined in the same way as the ionosphere-free observables.

Different standards for representing the PCO can confound the comparisons, so we adjust the manufacturer PVs to be consistent with the IGS14 PCOs:

$$PV = PV_{PCO-Manufacturer} - PV_{PCO-IGS14} + PV_{Manufacturer} \quad (3)$$

where the phase variations due the PCO (PV_{PCO}) are computed by projecting the offset onto the line-of-sight direction, **e**, using

$$PV_{PCO} = \mathbf{r} \cdot \mathbf{e} = x_{PCO} cos(el) cos(az) + y_{PCO} cos(el) sin(az) + z_{PCO} sin(el) \quad (4)$$

For azimuth averaged PVs, only the z-offset is retained, simplifying to

$$PV_{PCO} = z_{PCO} sin(el) \quad (5)$$

Figure 13 (left) shows the comparison of the GPS IIIA IGS14 PVs including our extension to the average PVs based on the published values. To aid in the comparison of the overall shape, the published PVs are shifted to align the 0-degree boresight value with the IGS14 value.

Figure 13 shows the difference between the ground-measured and extended IGS14 phase calibrations. In light of the different techniques used to establish these estimates, the general agreement of the patterns to within 4 mm below 14 deg boresight, and 15 mm overall, is quite encouraging. Two candidate explanations for the remaining differences are spacecraft multipath effects, which are unaccounted for in the manufacturer's antenna measurements; and the consistency constraints imposed on the IGS14 antenna calibrations. The ability to detect and correct for spacecraft multipath is clearly an important benefit of using in-flight calibrations. Transmitter calibration differences due to the reference frame constraint are less critical; because they will have very little effect on POD, when combined with in-flight receiving antenna calibrations that compensate for these systematic effects (Jäggi et al. 2010).

It is quite interesting to note, however, that the measured PVs are smooth across the 14-degree transition, whereas the extended GPS IIIA calibration has a noticeable shift in the slope before and after 14 degrees. This feature is not unique to our solution but is also evident in the IGS14 Block IIR-M/B and IIF PVs. Given that our extension has been developed to be consistent with the Block II extensions, this discrepancy may highlight a potential deficiency in the IGS14 PVs which is potentially a result of the the Block IIAs being used as the baseline for later Block II satellite extensions (Schmid et al. 2016). Thus, future work to develop calibrations referenced to the manufacturer-provided GPS IIIA

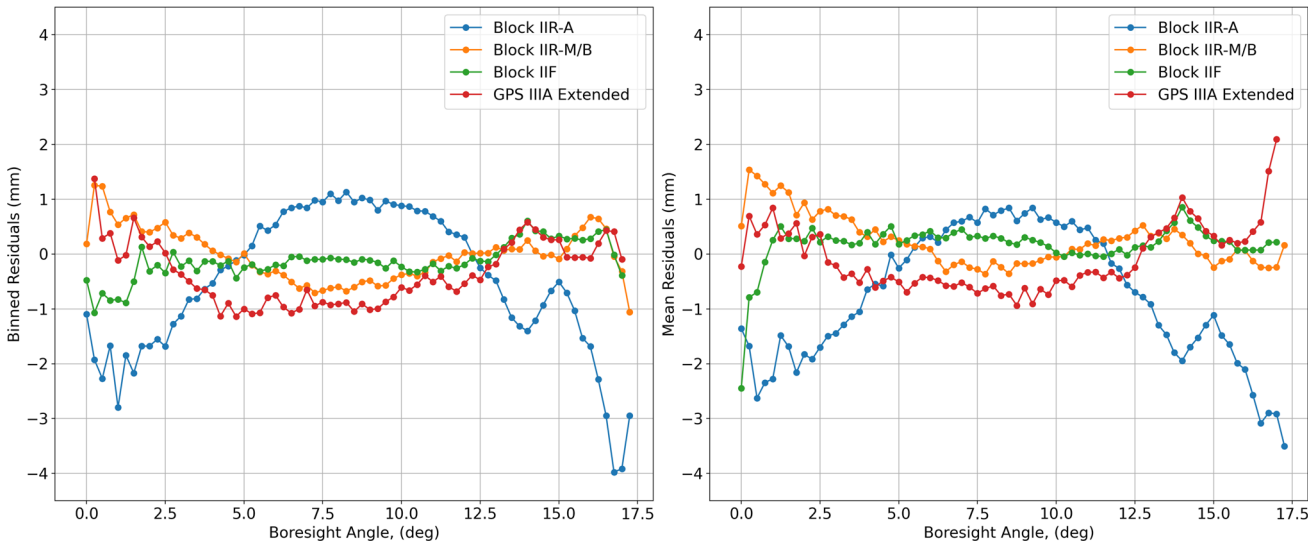

Fig. 12 Comparison of stacked block residuals by transmitter boresight angle for Sentinel-6 MF (left) and Jason-3 (right)

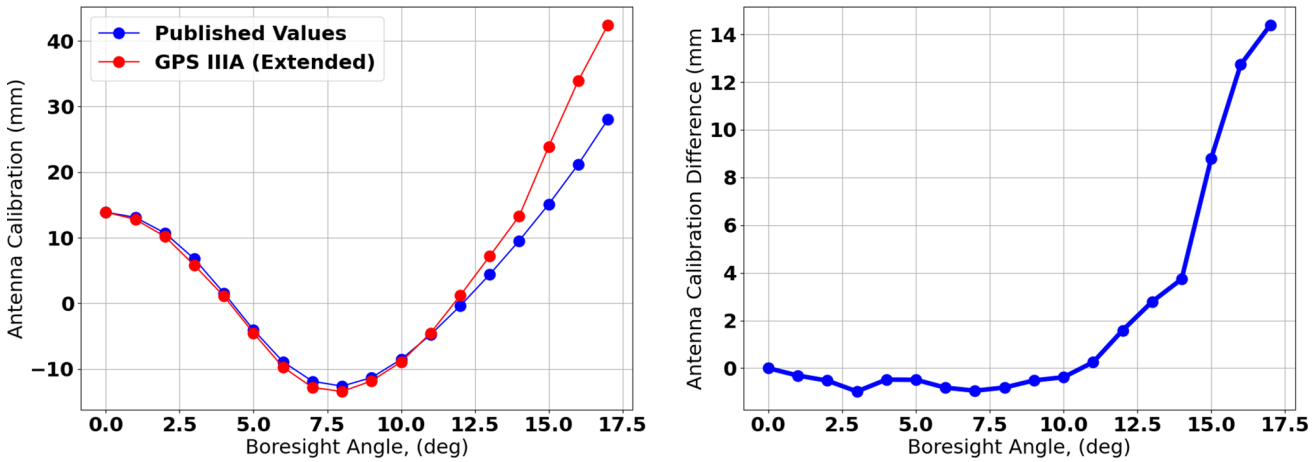

Fig. 13 Comparison of the average GPS IIIA manufacturer published phase variations to the extended IGS14 values (left) and the difference between them (right)

antenna patterns seems like a promising approach for further improvements in GPS performance.

5 Conclusion

The work presented demonstrates an effective extension of the IGS14 GPS IIIA PVs above 14-degree boresight angles and the resulting improvements to the orbit determination solutions for both Sentinel-6 MF and Jason-3. We provide a model for the GPS IIIA PVs for boresight angles greater than-14 degrees, and using an approach that makes them consistent with the IGS14 Block II PVs. Use of this GPS IIIA PV extension, determined only from Sentinel-6 tracking data, results in better consistency between orbit solutions determined from Block II-only tracking data and those including both Block II and III. Most metrics demonstrate improvements when using the combination of Block II and IIIA tracking data together with GPS IIIA PV extension, and degradation when using the original IGS14 GPS IIIA PVs as provided. POD solutions for low-Earth orbiters will likely be degraded without a more reliable antenna calibration for GPS IIIA satellites, with the impact continuing to grow as the number of GPS IIIA satellites increases. Our estimates for the GPS IIIA PVs for boresight angles greater than 14 degrees remove this potential degradation. Additionally, the correlated residuals between Sentinel-6 MF and Jason-3 suggest that the IGS14 antenna calibrations could be improved across all sub-block types. Given the performance and low multipath properties of the Sentinel-6 MF TriG receiver, it presents the possibility for use as a reference calibration for estimation of the entire GPS transmitter antenna calibration

separate from a predetermined reference frame. An approach similar to that performed by Haines et al. (2015) could provide additional insight for improvement of the transmitter calibrations.

The current form of the IGS2020 transmitter calibrations have adjusted the PCOs of all GPS transmitters to the IGS realization of the ITRF2020 while continuing to use the PVs from the IGS14 transmitter calibrations. Similarly, the GPS IIIA PV extensions from this work, relative to the IGS14 Block II transmitters, could also be applied to the IGS2020 transmitter calibrations.

Acknowledgements The work performed by SD and BH for this paper was performed at the Jet Propulsion Laboratory, California Institute of Technology under contract with the National Aeronautics and Space Administration. The work performed by AC was supported by the Jet Propulsion Laboratory, California Institute of Technology on Subcontract 1659402 to the University of Colorado. We would also like to thank the reviewers for their valuable comments and suggestions.

Author Contributions All authors contributed to the study concept and to editing and review of the manuscript. AC performed the data analysis and wrote the initial manuscript draft. SD, BH, and PA provided significant guidance supporting the technical work.

Data Availability The Jason-3 and Sentinel-6 GPS datasets analyzed during the current study are available from http://www.noaa.gov and https://search.earthdata.nasa.gov/search?q=sentinel-6, respectively. The Sentinel-6 MF pre-launch antenna calibration is available at https://sideshow.jpl.nasa.gov/pub/usrs/sentinel6/s6trig_prelaunchantennacalibration.tar.gz. The in-flight antenna calibration is available upon request from A. Conrad (alex.conrad@colorado.edu).

Declarations

Conflict of interest The authors declare that they have no competing interests.

References

Altamimi Z, Rebischung P, Métivier L et al (2016) ITRF2014: a new release of the international terrestrial reference frame modeling nonlinear station motions. J Geophys Res Solid Earth 121(8):6109–6131. https://doi.org/10.1002/2016JB013098

Auriol A, Tourain C (2010) DORIS system: the new age. Adv Space Res 46(12):1484–1496. https://doi.org/10.1016/j.asr.2010.05.015

Bertiger W, Bar-Sever Y, Christensen E et al (1994) GPS precise tracking of TOPEX/POSEIDON: results and implications. J Geophys Res Oceans 99(C12):449–464. https://doi.org/10.1029/94JC01171

Bertiger W, Desai SD, Dorsey A et al (2010) Sub-centimeter precision orbit determination with GPS for ocean altimetry. Mar Geodesy 33(S1):363–378. https://doi.org/10.1080/01490419.2010.487800

Bertiger W, Desai SD, Haines BJ et al (2010) Single receiver phase ambiguity resolution with GPS data. J Geodesy 84(5):327–337. https://doi.org/10.1007/s00190-010-0371-9

Bertiger W, Bar-Sever Y, Dorsey A et al (2020) GipsyX/RTGx, a new tool set for space geodetic operations and research. Adv Space Res 66(3):469–489. https://doi.org/10.1016/j.asr.2020.04.015

Bruinsma S, Thuillier G, Barlier F (2003) The DTM-2000 empirical thermosphere model with new data assimilation and constraints at lower boundary: accuracy and properties. J Atmos Solar Terr Phys 65(9):1053–1070. https://doi.org/10.1016/S1364-6826(03)00137-8

Conrad A, Axelrad P, Desai SD, et al (2022) Improved modeling of the solar radiation pressure for the Sentinel-6 MF spacecraft. In: Proceedings of the 35rd international technical meeting of the satellite division of the institute of navigation (ION GNSS+ 2022), September 2022

Desai SD, Ray RD (2014) Consideration of tidal variations in the geocenter on satellite altimeter observations of ocean tides. Geophys Res Lett 41(7):2454–2459. https://doi.org/10.1002/2014GL059614

Desai SD, Yuan DN (2006) Application of the convolution formalism to the ocean tide potential: results from the gravity recovery and climate experiment (GRACE). J Geophys Res Oceans. https://doi.org/10.1029/2005JC003361

Dietrich A, Ries P, Sibois AE, et al (2018) Reprocessing of GPS products in the IGS14 frame. In: AGU Fall Meeting Abstracts, pp G33C–0690

Donlon C, Cullen R, Giulicchi L, et al (2021a) Copernicus Sentinel-6 Michael Freilich satellite mission: Overview and preliminary in orbit results. In: 2021 IEEE international geoscience and remote sensing symposium IGARSS, IEEE, pp 7732–7735

Donlon C, Cullen R, Giulicchi L et al (2021) The Copernicus Sentinel-6 mission: enhanced continuity of satellite sea level measurements from space. Remote Sens Environ 258(112):395. https://doi.org/10.1016/j.rse.2021.112395

Fischer A (2022) GPS III Earth Coverage (EC) Antenna Patterns. Lockheed Martin Space, https://www.navcen.uscg.gov/sites/default/files/pdf/gps/GPS_ZIP/GPS_III_EC_Antenna_Patterns_SVN_74_75_76_77_78.pdf

Folkner WM, Williams JG, Boggs DH (2009) The planetary and lunar ephemeris DE 421. IPN Progr Rep 42(178):1–34

Haines BJ, Bar-Sever Y, Bertiger W et al (2004) One-centimeter orbit determination for Jason-1: new GPS-based strategies. Mar Geodesy 27(1–2):299–318. https://doi.org/10.1080/01490410490465300

Haines BJ, Bar-Sever YE, Bertiger W et al (2015) Realizing a terrestrial reference frame using the global positioning system. J Geophys Res Solid Earth 120(8):5911–5939. https://doi.org/10.1002/2015JB012225

Huang W, Männel B, Brack A et al (2022) Estimation of GPS transmitter antenna phase center offsets by integrating space-based GPS observations. Adv Space Res 69(7):2682–2696. https://doi.org/10.1016/j.asr.2022.01.004

Jäggi A, Dach R, Bock H, et al (2010) Extending the GPS satellite antenna patterns of the IGS to nadir angles beyond 14 using LEO data. In: AGU Fall Meeting, pp 13–17, http://acc.igs.org/antennas/sat-ant-pcv+leo_agu11.pdf

Johnston G, Riddell A, Hausler G (2017) The international GNSS service. In: Springer handbook of global navigation satellite systems. Springer: Cham, pp 967–982

Knocke P, Ries J, Tapley B (1988) Earth radiation pressure effects on satellites. In: Astrodynamics conference, p. 4292

Lemoine JM, Biancale R, Reinquin F, et al (2019) CNES/GRGS RL04 Earth gravity field models, from GRACE and SLR data. GFZ Data Services

Lockheed Martin (2019) SVN74 APC & ISC data release, January 2019

Milani A, Nobili AM, Farinella P (1987) Non-gravitational perturbations and satellite geodesy. Adam Hilger Ltd., Bristol

Montenbruck O, Schmid R, Mercier F et al (2015) GNSS satellite geometry and attitude models. Adv Space Res 56(6):1015–1029. https://doi.org/10.1016/j.asr.2015.06.019

Montenbruck O, Hackel S, Wermuth M et al (2021) Sentinel-6A precise orbit determination using a combined GPS/Galileo receiver. J Geodesy 95(9):1–17. https://doi.org/10.1007/s00190-021-01563-z

Pearlman MR, Noll CE, Pavlis EC et al (2019) The ILRS: approaching 20 years and planning for the future. J Geodesy 93(11):2161–2180. https://doi.org/10.1007/s00190-019-01241-1

Petit G, Luzum B (2010) IERS Conventions 2010 (IERS Technical Note; 36), Frankfurt am Main: Verlag des Bundesamts für Kartographie und Geodäsie, 179 pp. Tech. rep

Ray RD (2013) Precise comparisons of bottom-pressure and altimetric ocean tides. J Geophys Res Oceans 118(9):4570–4584. https://doi.org/10.1002/jgrc.20336

Rebischung P, Schmid R (2016) IGS14/igs14.atx: a new framework for the IGS products. In: AGU Fall Meeting 2016, American Geophysical Union, San Francisco, CA

Rothacher M, Schaer S, Mervart L, et al (1995) Determination of antenna phase center variations using GPS data. In: IGS Workshop Proceedings: Special Topics and New Directions, GeoForschungsZentrum Potsdam Germany, pp 205–220

Schmid R, Rothacher M, Thaller D et al (2005) Absolute phase center corrections of satellite and receiver antennas. GPS Solut 9(4):283–293. https://doi.org/10.1007/s10291-005-0134-x

Schmid R, Steigenberger P, Gendt G et al (2007) Generation of a consistent absolute phase-center correction model for GPS receiver and satellite antennas. J Geodesy 81(12):781–798. https://doi.org/10.1007/s00190-007-0148-y

Schmid R, Dach R, Collilieux X et al (2016) Absolute IGS antenna phase center model igs08.atx: status and potential improvements. J Geodesy 90(4):343–364. https://doi.org/10.1007/s00190-015-0876-3

Steigenberger P, Thoelert S, Montenbruck O (2020) Gps iii vespucci: results of half a year in orbit. Adv Space Res 66(12):2773–2785. https://doi.org/10.1016/j.asr.2020.03.026

Thoelert S, Steigenberger P, Montenbruck O et al (2019) Signal analysis of the first GPS III satellite. GPS Sol 23(4):1–11. https://doi.org/10.1007/s10291-019-0882-7

Tien J, Young L, Meehan T, et al (2010) Next generation of spaceborne GNSS receiver for radio occultation science and precision orbit determination. In: AGU Fall Meeting Abstracts, pp G51A–0661

Tien JY, Okihiro BB, Esterhuizen SX, et al (2012) Next generation scalable spaceborne GNSS science receiver. In: Proceedings of the 2012 international technical meeting of the institute of navigation, pp 882–914

Wu SC, Yunck TP, Thornton CL (1991) Reduced-dynamic technique for precise orbit determination of low earth satellites. J Guid Control Dyn 14(1):24–30. https://doi.org/10.2514/3.20600

Young L (2017) JPL GNSS receivers, past, present, and future. In: Proceedings: workshop on emerging technologies for autonomous space navigation. Pasadena, CA: Jet Propulsion Laboratory, NASA, https://www.nasa.gov/sites/default/files/atoms/files/session_1_-_5_jpl_space_receivers_technology_larry_young.pdf

Yunck T, Wu SC, Wu JT et al (1990) Precise tracking of remote sensing satellites with the global positioning system. IEEE Trans Geosci Remote Sens 28(1):108–116. https://doi.org/10.1109/36.45753

Yunck T, Bertiger W, Wu S et al (1994) First assessment of GPS-based reduced dynamic orbit determination on TOPEX/Poseidon. Geophys Res Lett 21(7):541–544. https://doi.org/10.1029/94GL00010